Tomography-based monitoring of isothermal snow metamorphism under advective conditions

Pirmin Philipp Ebner[1,2], Martin Schneebeli[2,*], and Aldo Steinfeld[1,*]

[1] *Department of Mechanical and Process Engineering, ETH Zurich, 8092 Zurich, Switzerland*

[2] *WSL Institute for Snow and Avalanche Research SLF, 7260 Davos-Dorf, Switzerland*

Abstract

Time-lapse X-ray microtomography was used to investigate the structural dynamics of isothermal snow metamorphism exposed to an advective airflow. The effect of diffusion and advection across the snow pores on the snow microstructure were analysed in controlled laboratory experiments and further elaborated on natural snowpacks. The 3D digital geometry obtained by tomographic scans was used in direct pore-level numerical simulations to determine the effective transport properties. The results showed that isothermal advection with saturated air have no influence on the coarsening rate that is typical for isothermal snow metamorphism. Isothermal snow metamorphism is driven by evaporation-deposition caused by the Kelvin effect and is the limiting factor independently of the transport regime in the pores.

Keywords: snow, isothermal, metamorphism, advection, transport properties, tomography

1. Introduction

Snow is a bi-continuous material consisting of fully connected ice and pore space (air) (Löwe et al. 2011). Because of the proximity to the melting point, the high vapour pressure causes a continuous recrystallization of the snow microstructure known as snow metamorphism, even under moderate temperature gradients (Pinzer et al, 2012; Domine et al. 2008). The microstructural changes of snow towards equilibrium under conditions of constant temperature are referred to as isothermal snow metamorphism

* Corresponding author. Email: aldo.steinfeld@ethz.ch and schneebeli@slf.ch

(Colbeck, 1997; Kaempfer and Schneebeli, 2007). This is a coarsening process whose driving force is the reduction of the surface free energy of the complex ice-air interface. The energy reduction is caused by mass transport processes such as vapour diffusion (Neumann et al., 2009), surface diffusion (Kingery, 1960b), volume diffusion (Kuroiwa, 1961), and grain boundary diffusion (Colbeck, 1997a, 1998, 2001; Kaempfer and Schneebeli, 2007). Viscous or plastic flow (Kingery, 1960a), and evaporation-condensation with vapour transport (German, 1996; Hobbs and Mason, 1963; Legagneux and Domine, 2005; Maeno and Ebinuma, 1983) are also suggested to play an important role. The Kelvin effect is seen as the driving force for isothermal snow metamorphism (Bader, 1939; Colbeck, 1980). Recent studies indicate that sublimation-deposition is the dominant contribution for temperatures close to the melting point, whereas surface diffusion dominates at temperatures far below the melting point in isothermal metamorphism (Vetter et al, 2010). Snow has a high permeability, which facilitates diffusion of gases and, under appropriate conditions, airflow (Gjessing, 1977; Colbeck, 1989; Sturm and Johnson, 1991; Waddington et al., 1996). Both diffusion and advective airflow affect heat and mass transports in the snow pack (Cunningham and Waddington, 1993; Albert, 1993; McConnell et al. 1998). In the dry snow zone of an ice sheet, Sowers et al. (1992) described a convective zone located just below the surface in which the air is rapidly flushed by convective exchange with the overlying atmosphere. A rapid decrease of the airflow velocity inside a snow layer (≤ 0.01 m s^{-1}) for high wind speed (≈ 10 m s^{-1}) above the snow surface (pore size ≈ 1 mm) are numerically estimated by Neumann (2003). In addition, Colbeck et al. (1997) confirmed the rapid decrease of airflow velocities inside a snow pack. It is suggested that advective flow of air has a direct effect on snow-air exchange processes related to atmospheric chemistry (Clifton et al., 2008; Grannas et al., 2007), and snow metamorphism (Albert and Gilvary, 1992; Albert et al., 2004), and can change the chemical composition of trapped atmospheric gases in ice-cores (Legrand and Mayewski, 1997; Neumann and Waddington, 2004; Severinghaus et al., 2010). However, no prior studies have experimentally analyzed the effect of saturated airflow on the vapour transport and the recrystallization of the snow crystals using non-destructive technique in time-lapse experiments. Over- or undersaturated air leads to a rapid growth or shrinkage of snow structures exposed to such conditions, as exemplified in the growth of surface hoar (Stössel et al., 2010). However, saturation vapour density of the air is reached in the pore space within the first 1 cm of the snow sample, regardless of temperature or flow rate (Neumann et al., 2009; Ebner et al., 2014). The change in shape of the snow crystals during metamorphism also affects the permeability, which, in turn, will continue to affect the shape of the snow structure. Although long-term isothermal metamorphism occurs in nature only in the centre of the polar ice caps (Arnaud et al., 1998), it is important to reduce physical complexity of experiments in order to understand the basic mechanisms governing metamorphism.

The objective of this paper is to study the effect of saturated airflow on the vapour transport and the coarsening rate of snow under isothermal conditions. We designed experiments in a controlled refrigerated laboratory and used time-lapse computed tomography (micro-CT) to obtain the discrete-scale geometry of snow (Schneebeli and Sokratov, 2004; Kaempfer and Schneebeli, 2007; Pinzer and Schneebeli, 2009; Chen and Baker, 2010; Pinzer et al., 2012; Wang and Baker, 2014; Ebner et al., 2014). The extracted 3-D digital geometry of the snow was used to calculate the specific surface area and porosity. Direct pore-level simulations (DPLS) were applied to determine the effective permeability by solving the corresponding mass and momentum conservation equations (Zermatten et al., 2011, 2014).

2. Methodology

Isothermal experiments with fully saturated airflow across snow samples were performed in a micro-CT (Ebner et al., 2014) at laboratory temperatures of T_{lab} = −8 and −15 ºC. Figure 1 shows a schematic of the experimental setup. Two different snow types with high specific surface area were considered to evaluate the structural change in the earlier stage of isothermal metamorphism of new snow, more in detail. Natural identical snow was used for the snow sample preparation (water temperature: 30 ºC; air temperature: −20 ºC) (Schleef et al., 2014). It was sieved with a mesh size of 1.4 mm into two boxes, and sintered for 13 and 27 days at −15 and −5 ºC, respectively, for increasing strength and coarsening (Kaempfer and Schneebeli, 2007). A cylinder cut out (diameter: 53 mm; height: 30 mm) from the sintered snow was filled into the sample holder (Ebner et al., 2014). The snow samples were analysed during 96 h with time-lapse micro-CT measurements taken every 8 h, producing a sequence of 13 images. Four different runs were chosen based on the Peclet number ($Pe = u_D d_p/D$ where u_D is the superficial velocity in snow, d_p is the pore diameter, and $D = 2.036 \cdot 10^{-5}$ m^2 s^{-1} is the diffusion coefficient of water vapour in air) to compare the advective and diffusive transport rates inside the pore space. Experimental runs were performed at 1 atm pressure and volume flow rates of 0 (no advection), 0.36, 3.0, and 5.0 L min^{-1}, corresponding to *Pe* = 0, 0.05, 0.47, and 0.85. Higher *Pe* numbers were experimentally not possible, as the shear stress by airflow could destroy the snow structure and we restricted the flow rate to the corresponding maximum *Pe* ≈ 0.8 extracted from the simulation of Neumann (2003) and Colbeck (1997). Assuming an isothermal snowpack, *Pe* > 1 is unlikely in nature because of: 1) low density snow, which has always a very low strength, will be destroyed due to the high airflow velocity; 2) *Pe* > 1 would be possible for depth hoar, but this snow type is typically found at depth and rarely exposed to high windspeed (Colbeck, 1997); 3) *Pe* depends on the temperature due to changing diffusivity. Seasonal temperature fluctuations of -60 ºC to -30 º C are typical for surface snow layer in Antarctic regions, and lead to *Pe* variations of up to 25%. Theoretically, *Pe* ≈ 1.2 could be realistic at -60 ºC for 'sa4'. However, simulations by Neumann (2003) showed a rapid decrease of the airflow velocity inside the snow layer (≤ 0.01 m s^{-1}) for a high wind speed (≈ 10 m s^{-1}) above the snow surface (pore size ≈ 1 mm). This leads to a maximum *Pe* ≈ 0.8. Table 1 summarizes the experimental conditions.

The acceleration voltage in the X-ray tube was 70 kV, with an intensity of 114 μA, and a nominal resolution of 18 μm. The samples were scanned with 2000 projections per 360 degree, with an integration time of 200 ms per projection, taking 1.5 hour per scan. The innermost 36.9 mm of the total 53 mm diameter were scanned and subsamples with a dimension of 7.2 × 7.2 × 7.2 mm^3 were extracted for further processing. Absolute *z*-position varied up to a maximum of 50 voxels between subsequent scans due to the weight of the sample holder. To correct for the *z*-position a linear encoder was built into the micro-CT. A 3×3×3 median filter and Gaussian filter (σ = 1.4, support = 3) was applied to the reconstructed images. Otsu's method (Otsu, 1979) was used to automatically perform clustering-based image thresholding to segment the grey-level images into ice and air phase. Morphological properties in the two-phase system were determined based on the geometry obtained by the micro-CT. The segmented data were used to calculate a triangulated ice matrix surface and tetrahedrons inscribed into the ice structure. Morphological parameters such as porosity (ε) and specific surface area (SSA) were then calculated. The effective permeability was calculated using the finite volume technique CFD (Computational Fluid Dynamics simulation software from ANSYS) by solving the continuity and Navier–Stokes equations (Zermatten et al., 2011, 2014) for laminar flow

$$\nabla p = -\frac{\mu}{K} u_{\mathrm{D}} - F \rho u_{\mathrm{D}}^2 - \frac{\gamma \rho^2}{\mu} u_{\mathrm{D}}^3 \quad (1)$$

where p is the pressure, μ is the dynamic viscosity of the fluid and u_D its superficial velocity, ρ is the fluid density, K is the permeability, F is the Dupuit-Forchheimer coefficient, and γ is a dimensionless factor. The first term is the result of viscous effects, predominant at low velocities, whereas the second and third terms describe the inertial effects, which become important at higher fluid velocities. As the viscous effect was still the dominant case (Re ≈ 1) in the experiment, only permeability K was considered for further discussions. A grid convergence study based on the pressure drop (Zermatten et al., 2014) was carried out to find the optimal representative elementary volume (REV) (6.0 x 6.0 x 3.0 mm^3). An in-house tetrahedron-based mesh generator (Friess et al. 2013) was used to create the computational grid on the segmented data. The computational domain consisted of a square duct containing a sample of snow. The boundary conditions consisted of uniform inlet velocity, temperature and outlet pressure, constant wall temperature at the solid-fluid interface, and symmetry of the sample at the lateral duct walls. The square duct was 5 times the length of the sample to ensure a fully developed velocity profile at the entrance of the snow sample (Fig. 2). The largest mesh element length was 0.153 mm and the smallest possible mesh element measured 9.56 µm, with average 60 million volume elements for each segmented snow sample.

3. Results and Discussion

The discussions of the observed results are only based on the investigated volume. Influences of the flow on the base, top and lateral boundaries of the overall sample were not considered due to lack of structural observations.

A representative temporal temperature profile of the snow sample for both laboratory temperatures of T_{lab} = -8 ˚C and -15 ˚C is shown in Figure 3. Variations in temperature up to 1.7 ˚C and 1.4 ˚C were due to heat dissipated by the X-ray tube and temperature fluctuations inside the cold laboratory (Ebner et al., 2014). A longer sintering duration at higher temperature of the snow for experiment 'sa3' and 'sa4' was used to increase the mean thickness of the ice matrix. This avoided the destruction of the snow structure due to shear stresses caused by the airflow. The structural analysis of the snow samples was conducted on the complete tomography domain (7.2 × 7.2 × 7.2 mm^3). A smaller sub-set of 110 × 42 × 110 voxels (2 × 0.75 × 2 mm^3) was selected to visualize the 3D evolution (Fig. 4). It showed no significant change in the grain shape, even for different airflow velocities, and only a slight rounding and coarsening was seen for experiments ‘sa1’ and ‘sa2’. A strong translation effect due to settling of sub-layering snow was visible for ‘sa1’ and ‘sa2’. The initial ice grain didn’t change with time; only coarsening processes on the ice grain surface were observed (Fig. 5). Sublimation of 4.5 % and 4.9 % of the ice matrix and deposition of 4.1 % and 5.9 % on the ice matrix were observed for ‘sa3’ and ‘sa4’ (Fig. 6). The data were extracted by superposition of vertical cross-sections at 0 and 96 hours with an uncertainty of 6 %. The mass sublimated preferentially at locations of the ice grain with low radii due to Kelvin-effect and was relocated on the grain leading to a smoothing of the ice grain. The airflow velocity did not affect the relocation process.

The well-sintered snow showed very little settling under its own weight (Kaempfer and Schneebeli, 2007) and, consequently, no significant change in porosity was observed. This supports the hypothesis that further densification is limited by coarsening kinetics (Kaempfer and Schneebeli, 2007, Schleef et al., 2013). A spatially constant porosity distribution at t = 0 days and t = 4 days is seen in Fig. 7. Thus, spatial change in the flow field due to different interfacial velocities can be neglected. Consequently, Pe was constant with time, and therefore the advective and diffusive mass transfer regime. The average deviation between t = 0 days and t = 4 days was 0.5%, 1.8%, 0.5% and 0.5% for ‘sa1’, ‘sa2’, ‘sa3’ and ‘sa4’.

Our segmented 3D-data accurately reproduced the original snow sample and the temporal porosity distribution confirmed that no settling and densification occurred in the investigated volume (Fig. 8). The gravimetric porosity ε_{grav} at the beginning and at the end of each experiment was measured by weighing. The measured density values were converted to porosity ($\varepsilon_{grav} = 1-\rho_s/\rho_{ice}$), and compared to the value of porosity computed by DPLS on the micro-CT geometry. The computed values differed from the measured ones by 1.4% and 0.1% at the beginning and 4.1% and 2.3% at the end for experiments ‘sa3’ and ‘sa4’.

The qualitative progression of the spatial SSA of the scanned snow height for four discs of 7.2 × 7.2 × 1.8 mm^3 (Fig. 9) did not change significantly with height. This suggested that the snow properties were homogeneous throughout the sample and duration of the experiments. The slight decrease of the spatial SSA for experiment ‘sa4’ is explained by the distribution not initially being completely homogeneous.

The coarsening process led to a decrease of the SSA over time (Fig. 10), which was higher for group ‘sa1’ and ‘sa2’ compared to ‘sa3’ and ‘sa4’. The difference was caused by the 34% lower initial SSA of group ‘sa3’ and ‘sa4’. Applying the theories developed by Legagneux et al. (2004) and Legagneux and Domine (2005), the evolution of SSA of the ice matrix could be modelled well. The model proposed is given by (Legagneux and Domine, 2005)

$$\mathrm{SSA} = \mathrm{SSA}_0 \left(\frac{\tau}{\tau + t} \right)^{1/n} \tag{2}$$

where SSA_0 is the initial SSA at time $t = 0$, n is the growth exponent, and τ a parameter related to grain growth and a form factor. Table 2 shows the fitted parameters and the corresponding normalized root-mean square error (NRMSE) for each experiment. Equation (2) fits the data of each experiment well with an average NRMSE < 0.21. The computed fit of the SSA is shown in Figure 8. Equation (2) gives a very qualitative estimation on the real mechanism occurring in the snow. This model is based on the physical processes involved in Ostwald ripening (Ratke and Voorhees, 2002). Ostwald ripening describes the coarsening of solid particles with a given size distribution, considering disconnected grains that do not undergo settling. The driving force in the model is the reduction of the SSA and the model hypothesis is based on the concept that mass transfer occurs by sublimation due to curvature effects, transport through the gas phase and deposition. Theoretically, the growth exponent n is approximately 2 when surface processes are rate limiting and 3 when diffusion is rate limiting. Experiment ‘sa1’ and ‘sa2’ had a higher value of n, indicating a strong coarsening process due to sintering and that surface processes were rate limiting (Legagneux et al., 2004; Legagneux and Domine, 2005). Experiment ‘sa1’ and ‘sa2’, and ‘sa3’ and ‘sa4’ had similar fitting parameters and a low value of n, suggesting that surface effects were rate limiting. The lower value of n for experiment ‘sa3’ and ‘s4’ was due to the longer sintering time of 27 days at -5 ºC before the experiments were started leading to a very little change in the microstructure of the snow. When the sintering times of 13 and 27 days were included in the model, the fitting parameters indicated a consistent growth exponent n for each experiment (Table 3) and a good agreement with the theory. They expressed strong coarsening and surface processes for each experiment. Notice, Eq. (2) extremely depends on the initial state, which is well illustrated by the large difference obtained for n values of ‘sa3’ and 'sa4' between Tables 2 and 3. Concluding, the calculated values indicated that surface processes caused the limiting rate rather than the diffusion step and no significant influence of advective transport could be observed.

The effect of decreasing SSA on the permeability was not elucidated in our experiments. A SSA decrease of at least 5% in the experiments could not be reproduced in the permeability. However, the computational uncertainty up to 16% (Zermatten et al., 2014) in the permeability is still in the range to cover the correlation between SSA and permeability. The effect of increasing airflow velocity had no influence on the flow characteristics (Fig. 11). The temporal evolution of permeability for experiment 'sa2' showed a decrease of 8% for the first 40 hours and remained constant afterwards. Experiments 'sa1', 'sa3' and 'sa4' showed no significant change in the permeability, which is consistent with the negligible change in density. The average fluctuations of the permeability K between each time step and the slight decrease at the beginning in 'sa2' showed small differences that were below the precision of the numerical method with an uncertainty up to 16% (Zermatten et al., 2014). Only the first time step of 'sa3' showed a particularly high difference of 17.3%, but neither the porosity nor SSA showed significant differences reflecting this value. This difference could therefore be due to an error during the measurement.

4. Summary and conclusions

Four isothermal metamorphism experiments of snow under saturated advective airflow were performed, each with duration of four days. The two main transport processes, diffusion and advection, were analysed inside the pore space. The airflow velocities were chosen based on the Peclet number. $Pe > 0.85$ were not possible due to the destruction of the snow structure and is not realistic in natural snowpacks. Every 8 h the snow microstructure was observed by X-ray micro-tomography. The micro-CT scans were segmented, and porosity and specific surface area were calculated. Effective permeability was calculated in direct pore-level simulations (DPLS) to analyse the flow characteristic.

The experimental observations supported the hypothesis that further densification was limited by coarsening kinetics and further confirmed a constant porosity evolution (Kaempfer and Schneebeli, 2007). Curvature caused sublimation of small ice grains and ice structures with small surface radii leading to a slight decrease in SSA. Compared to rates typical for isothermal snow metamorphism, no enhancement of mass transfer inside the pores of isothermal advection with saturated air was observed. Evaporation-deposition caused by the Kelvin-effect was the limiting factor independently of the transport regime in the pores.

Acknowledgements

The Swiss National Science Foundation granted financial support under project Nr. 200020-146540. The authors thank M. Jaggi and S. Grimm for technical support with the measurements.

References

Albert, M. R. and Mc Gilvary, W. R.: Thermal effects due to air flow and vapour transport in dry snow, Journal of Glaciology, 38, 274–281, 1992.

Albert, M. R.: Numerical experiments on firn ventilation with heat transfer, Annals of Glaciology, 18, 161–165, 1993.

Albert, M. R., Shuman, C., Courville, Z., Bauer, R., Fahnestock, M., and Scambos, T.: Extreme firn metamorphism: impact of decades of vapor transport on near-surface firn at a low-accumulation glazed site on the east Antarctic plateau, Annals of Glaciology, 39, 73–78, 2004.

Ansys, 2010: Ansys-CFX. In: A. Inc. (Ed.), (Canonsburg, PA).

Arnaud, L., Lipenkov, V., Barnola, J., Gay, M., and Duval, P.: Modelling of the densification of polar firn: characterization of the snow-firn transition, Annals of Glaciology, 26, 39–44, 1998.

Bader, H., Haefeli, R., Bucher, E., Neher, J., Eckel, C., and Thams, C.: Der Schnee und seine Metamorphose, Beitr. Geologie der Schweiz, Geotechnische Serie-Hydrologie, 3, 1–313, 1939.

Chen, S. and Baker, I.: Evolution of individual snowflakes during metamorphism, Journal of Geophysical Research, vol. 115, 1–9, 2010.

Clifton, A., Manes, C., Rüedi, J.-D., Guala, M., and Lehning, M.: On shear-driven ventilation of snow, Boundary-Layer Meteorology, 126, 249–261, 2008.

Colbeck, S. C.: Thermodynamics of snow metamorphism due to variations in curvature, Journal of Glaciology, 26, 291–301, 1980.

Colbeck, S. C.: Air movement in snow due to wind-pumping, Journal of Glaciology, 35, 209–213, 1989.

Colbeck, S. C.: A review of sintering in seasonal snow, Technical Report, 97-10, Cold Regions Research & Engineering Laboratory, Hanover, New Hampshire, 1997.

Colbeck, S. C.: Model of wind pumping for layered snow, Journal of Glaciology, 43, 60–65, 1997.

Colbeck, S. C.: Sintering in a dry snow cover, Journal of Applied Physics, 84, 4585–4589, 1998.

Colbeck, S. C.: Sintering of unequal grains, Journal of Applied Physics, 89, 4612–4618, 2001.

Cunningham, J. and Waddington, E. D.: Air flow and dry deposition of non-sea salt sulphate in polar firn: paleoclimatic implications, Atmospheric Environment, 27A, 2943–2956, 1993.

Domine, F., M. Albert, T. Huthwelker, H.-W. Jacobi, A. A. Kokhanovsky, M. Lehning, G. Picard, and W. R. Simpson: Snow physics as relevant to snow photochemistry, Atmos. Chem. Phys., 8, 171–208, 2008.

Ebner, P. P., Grimm, A. S., Schneebeli, M., and Steinfeld, A.: An instrumented sample holder for time-lapse micro-tomography measurements of snow under advective conditions, Geoscientific Instrumentation Methods and Data Systems, 3, 179–185, 2014.

Friess, H., Haussener, S., Steinfeld, A., and Petrasch, J.: Tetrahedral mesh generation based on space indicator functions, International Journal for Numerical Methods in Engineering, 93, 1040–1056, 2013.

German, R. M.: Sintering Theory and Practive, John Wiley, New York, 1996.

Gjessing, Y. T.: The filtering effect of snow. In: Oeschger, H., Ambach, W., Junge, C. E., Lorius, C., and Serebryanny, L. (Eds.): Isotopes and Impurities in Snow and Ice Symposium, 118, IASH-AISH Publication, Dorking, 199–203, 1977.

Grannas, A. M., *and 34 others*: An overview of snow photochemistry: evidence, mechanisms and impacts, Atmospheric Chemistry and Physics, 7, 4329–4373, 2007.

Hobbs, P. V. and Mason, B. J.: The sintering and adhesion of ice, Philosophical Magazine, 9, 181–197, 1963.

Kaempfer, T. U. and Schneebeli, M.: Observation of isothermal metamorphism of new snow and interpretation as a sintering process, Journal of Geophysical Research, 112, 1–10, 2007.

Kingery, W. D.: On the metamorphism of snow, in International Geological Congress, XXI Sesion, Norden, Copenhagen, 81–89, 1960a.

Kingery, W. D.: Regelation, surface diffusion, and ice sintering, Journal of Applied Physics, 31, 833–838, 1960b.

Kuroiwa, D.: A study of ice sintering, Tellus, 13, 252–259, 1961.

Legagneux, L. and Domine, F.: A mean field model of the decrease of the specific surface area of dry snow during isothermal metamorphism, Journal of Geophysical Research, 110, F04011, doi:10.1029/2004JF000181, 2005.

Legagneux, L., Taillandier, A. S., and Domine, F.: Grain growth theories and the isothermal evolution of the specific surface area of snow, Journal of Applied Physics, 95, 6175–6184, 2004.

Legrand M. and Mayewski P.: Glaciochemistry of polar ice cores: A review, Reviews of Geophysics, 35, 219–243, 1997.

Löwe, H., Spiegel, J. K., and Schneebeli, M.: Interfacial and structural relaxations of snow under isothermal conditions, J. Glaciology, 57, 499–510, 2011.

McConnell, J. R., Bales, R. C., Stewart, R. W., Thompson, A. M., Albert, M. R., and Ramos, R.: Physically based modelling of atmosphere-to-snow-to-firn transfer of H_2O_2 at the South Pole, Journal of Geophysical Research, 103, 10561–10570, 1998.

Maeno, N. and Ebinuma, T.: Pressure sintering of ice and its implication to the densification of snow at polar glaciers and ice sheets, Journal of Physical Chemistry, 87, 4103–4110, 1983.

Neumann, T. A.: Effects of firn ventilation on geochemistry of polar snow, (PhD thesis, University of Washington), 2003.

Neumann, T. A. and Waddington, E. D.: Effects of firn ventilation on isotopic exchange, Journal of Glaciology, 50, 183–194, 2004.

Neumann, T. A., Albert, M. R., Engel, C., Courville, Z., and Perron, F.: Sublimation rate and the mass transfer coefficient for snow sublimation, International Journal of Heat and Mass Transfer, 52, 309–315, 2009.

Otsu, N.: A Threshold Selection Method from Gray-Level Histograms, IEEE Transactions on Systems Man and Cybernetics, 9, 62–66, 1979.

Pinzer, B. R. and Schneebeli, M.: Breeding snow: an instrumented sample holder for simultaneous tomographic and thermal studies, Measurement Science and Technology, 20, 1–9, 2009.

Pinzer, B. R., Schneebeli, M., and Kaempfer, T. U.: Vapor flux and recrystallization during dry snow metamorphism under a steady temperature gradient as observed by time-lapse micro-tomography, The Cryosphere, 6, 1141–1155, 2012.

Ratke, L. and Voorhees, P. W.: Growth and Coarsening, Springer, ISBN 3-540-42563-2, 2002.

Schleef, S. and Löwe, H.: X-ray microtomography analysis of isothermal densification of new snow under external mechanical stress, Journal of Glaciology, 59, 233–243, 2013.

Schleef, S., Jaggi, M., Löwe, H., and Schneebeli, M.: Instruments and Methods: An improved machine to produce nature-identical snow in the laboratory, Journal of Glaciology, 60, 94–102, 2014.

Schneebeli, M. and Sokratov, S.: Tomography of temperature gradient metamorphism of snow and associated changes in heat conductivity, Hydrological Processes, 3665, 3655–3665, 2004.

Severinghaus, J. P., Albert, M. R., Courville, Z. R., Fahnestock, M. A., Kawamura, K., Montzka, S. A., Muehle, J., Scambos, T. A., Shields, E., Shuman, C. A., Suwa, M., Tans, P., and Weiss, R. F.: Deep air convection in the firn at a zero-accumulation site, central Antarctica, Earth and Planetary Science Letters, 293, 359–367, 2010.

Sowers, T., Bender, M., Raynard, D., and Korotkevich, Y. S.: δ15N in air trapped in polar ice: a tracer of gas transport in the firn and a possible constraint on ice age-gas age differences, Journal of Geophysical Research, 97, 15683–15697, 1992.

Stössel, F., Guala, M., Fierz, C., Manes, C., and Lehning M.: Micrometeorological and morphological observations of surface hoar dynamics on a mountain snow cover, Water Resources Research, 46, 1–11, 2010.

Sturm, M. and Johnson, J. B.: Natural convection in the subarctic snow cover, Journal of Geophysical Research, 96, 11657–11671, 1991.

Vetter, R., S. Sigg, H. M. Singer, D. Kadau, H. J. Herrmann, and M. Schneebeli, Simulating isothermal aging of snow, EPL (Europhysics Lett.), 89(2), 26001, doi:10.1209/0295-5075/89/26001, 2010.

Waddington, E. D., Cunningham, J., and Harder, S. L.: The effects of snow ventilation on chemical concentrations. In: Wolff, E. W. and Bales, R. C. (Eds.), Chemical Exchange Between the Atmosphere and Polar Snow, NATO ASI Series, 43, Springer, Berlin, 403–452, 1996.

Wang, X. and Baker, I.: Evolution of the specific surface area of snow during high-temperature gradient metamorphism, Journal of Geophysical Research Atmospheres, vol. 119, 13690 – 13703, 2014.

Zermatten, E., Haussener, S., Schneebeli, M., and Steinfeld, A.: Instruments and Methods: Tomography-based determination of permeability and Dupuit-Forchheimer coefficient of characteristic snow samples, Journal of Glaciology, 57, 811–816, 2011.

Zermatten, E., Schneebeli, M., Arakawa, H., and Steinfeld, A.: Tomography-based determination of porosity, specific area and permeability of snow and comparison with measurements, Cold Regions and Technology, 97, 33–40, 2014.

Table 1: Morphological and flow characteristics of the experiments: Volume flow ($\dot{V}$), corresponding Peclet number (Pe), Reynolds number (Re), initial superficial velocity in snow ($u_{D,0}$), initial snow density (ρ_0) ~~(± 7.7 %)~~, initial porosity (ε_0) ~~(± 7.7 %)~~, specific surface area (SSA_0) ~~(± 18.8 %)~~, initial pore diameter (d_p), temperature in the cold laboratory (T_{lab}), and the sintering time of the snow.

Name	$\dot{V}$ litre min^{-1}	Pe –	Re –	$u_{D,0}$ m s^{-1}	ρ_0 kg m^{-3}	ε_0 –	SSA_0 m^2 kg^{-1}	d_p mm	T_{lab} ˚C	Sintering time
sa1	–	–	–	–	226.43	0.75	46.6	0.22	-8.0	13 days at -15˚C
sa2	0.36	0.05	0.07	0.004	186.1	0.78	43.7	0.27	-8.0	13 days at -15˚C
sa3	3.0	0.47	0.6	0.04	325.43	0.65	28.7	0.24	-15.0	27 days at -5˚C
sa4	5.0	0.85	1.1	0.06	264.93	0.71	28.0	0.29	-15.0	27 days at -5˚C

Table 2: Values of the fitted growth rate τ and growth exponent n for the evolution of the SSA and the corresponding normalized root-mean square error (NRMSE).

Name	SSA_0 m^2 kg^{-1}	τ –	n –	NRMSE –
sa1	46.7	632.9	2.10	0.01
sa2	43.6	721.2	2.15	0.04
sa3	27.8	14400	0.32	0.14
sa4	27.8	17380	0.39	0.21

Table 3: Values of the fitted growth rate τ and growth exponent n for the evolution of the SSA including the sintering time of 13 and 27 days, and the corresponding normalized root-mean square error (NRMSE).

Name	SSA_0 m^2 kg^{-1}	τ –	n –	NRMSE –
sa1	64.4	320.9	2.10	0.01
sa2	56.8	409.1	2.15	0.04
sa3	34.5	1229	2.0	0.15
sa4	36.0	1063	1.91	0.27

Figure captions

Fig. 1. Schematic of the experimental setup and the sample holder. A thermocouple (TC) and a humidifier sensor (HS) inside the humidifier measured the airflow conditions. Two thermistors (NTC) close to the snow surface measured the inlet and outlet temperature of the airflow (Ebner et al., 2014).

Fig. 2. Schematic of the computational domain with an enlarged subsample of snow. In the snow sample, the dark gray part represents the ice, whereas the mesh is built in the pore space.

Fig. 3. A typical temperature profile for experiment 'sa1, sa2' and 'sa3, sa4'. The temperature rise was caused by the X-ray tube and fluctuations inside the cold laboratory (Ebner et al., 2014). The accurateness of the isothermal conditions between the top and base of the sample throughout the experiment is less than 0.2 ºC (Ebner et al., 2014).

Fig. 4. Evolution of the 3-D structure of the ice matrix during isothermal metamorphism under advective conditions. Experimental conditions (from left to right) at different measurement times from beginning to the end (top to bottom) of the experiment. The shown cubes are 110 × 42 × 110 voxels ($2 \times 0.75 \times 2$ mm^3) large.

Fig. 5. Residence time of ice particles within in a slice (5.7×5.7 mm^2) parallel to the flow direction for a) 'sa3' and b) 'sa4' by overlapping time-lapse tomography pictures. The period of 8 h was sufficiently short to calculate the residence time of each ice voxel with an uncertainty of 6 %.

Fig. 6. Superposition of vertical cross-section parallel to the flow direction at time 0 and 96 hours for (a) 'sa3' and (b) 'sa4'. Sublimation and deposition of water vapor on the ice grain were visible with an uncertainty of 6 %.

Fig. 7. Spatial porosity profile of the scanned area at the beginning and at the end of each experiment. The spatial variability within the reconstructed volume was measured in four discs of $7.2 \times 7.2 \times 1.8$ mm^3.

Fig. 8. Evolution of the porosity over time obtained by triangulated structure surface method and the measured gravimetric density (ε_{grav}) at the beginning and at the end of 'sa3' and 'sa4'.

Fig. 9. Spatial SSA profile of the scanned area at the beginning and at the end of each experiment. The spatial variability within the reconstructed volume was measured in four discs of 7.2 × 7.2 × 1.8 mm^3.

Fig. 10. Temporal evolution of the specific surface area, SSA, of the ice matrix obtained by triangulated structure surface method. The computed fit is of the form $\mathrm{SSA}(t) = \mathrm{SSA}_0 \left(\frac{\tau}{\tau + t}\right)^{1/n}$.

Fig. 11. Temporal evolution of the effective permeability by applying DPLS with an uncertainty of 16 % (Zermatten et al., 2014).

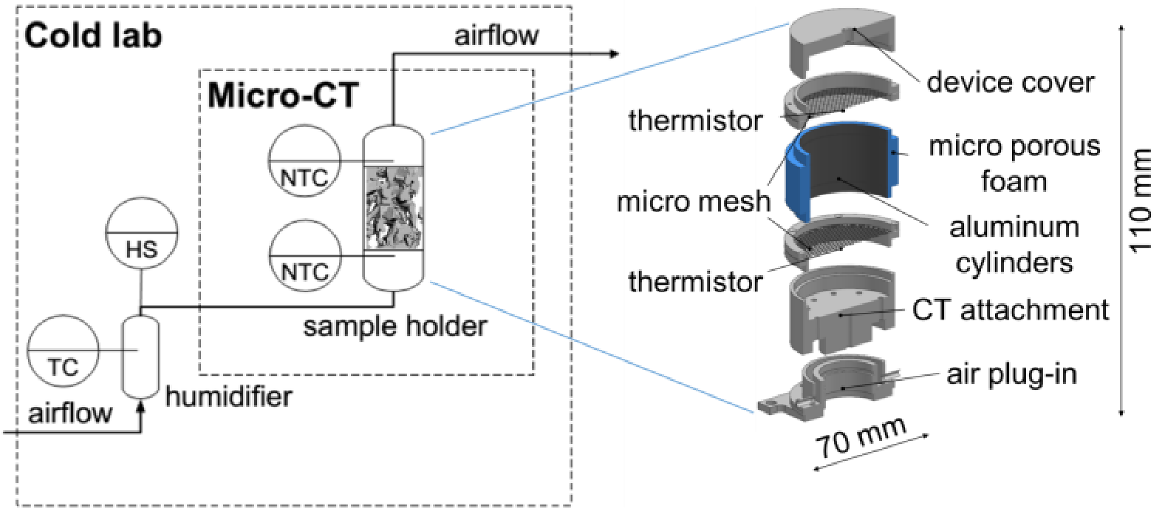
Cold lab
airflow
Micro-CT
NTC
NTC
HS
TC
airflow
humidifier
sample holder
device cover
thermistor
micro porous
foam
micro mesh
aluminum
cylinders
thermistor
CT attachment
air plug-in
110 mm
70 mm

Fig. 1

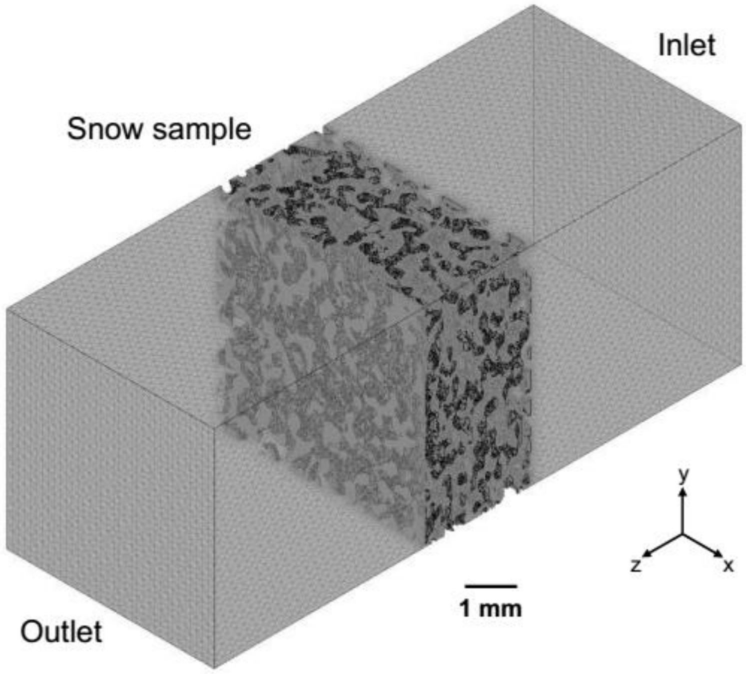

Fig. 2

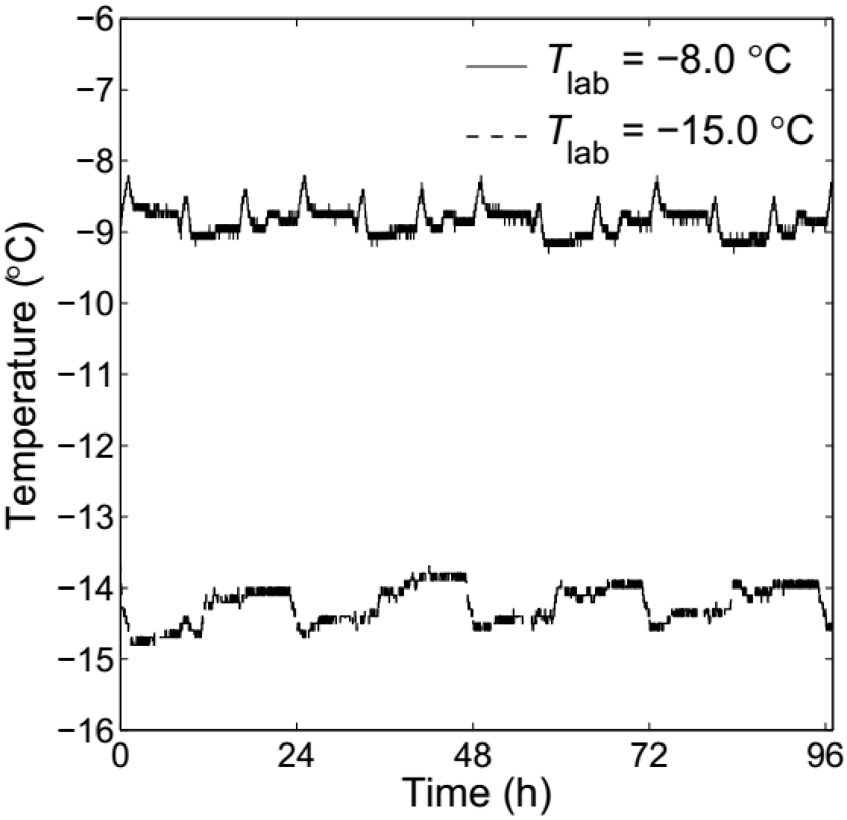
−6
−7
−8
−9
−10
−11
−12
−13
−14
−15
−16
0
24
48
72
96
Temperature (°C)
Time (h)
T_{lab} = −8.0 °C
T_{lab} = −15.0 °C

Fig. 3

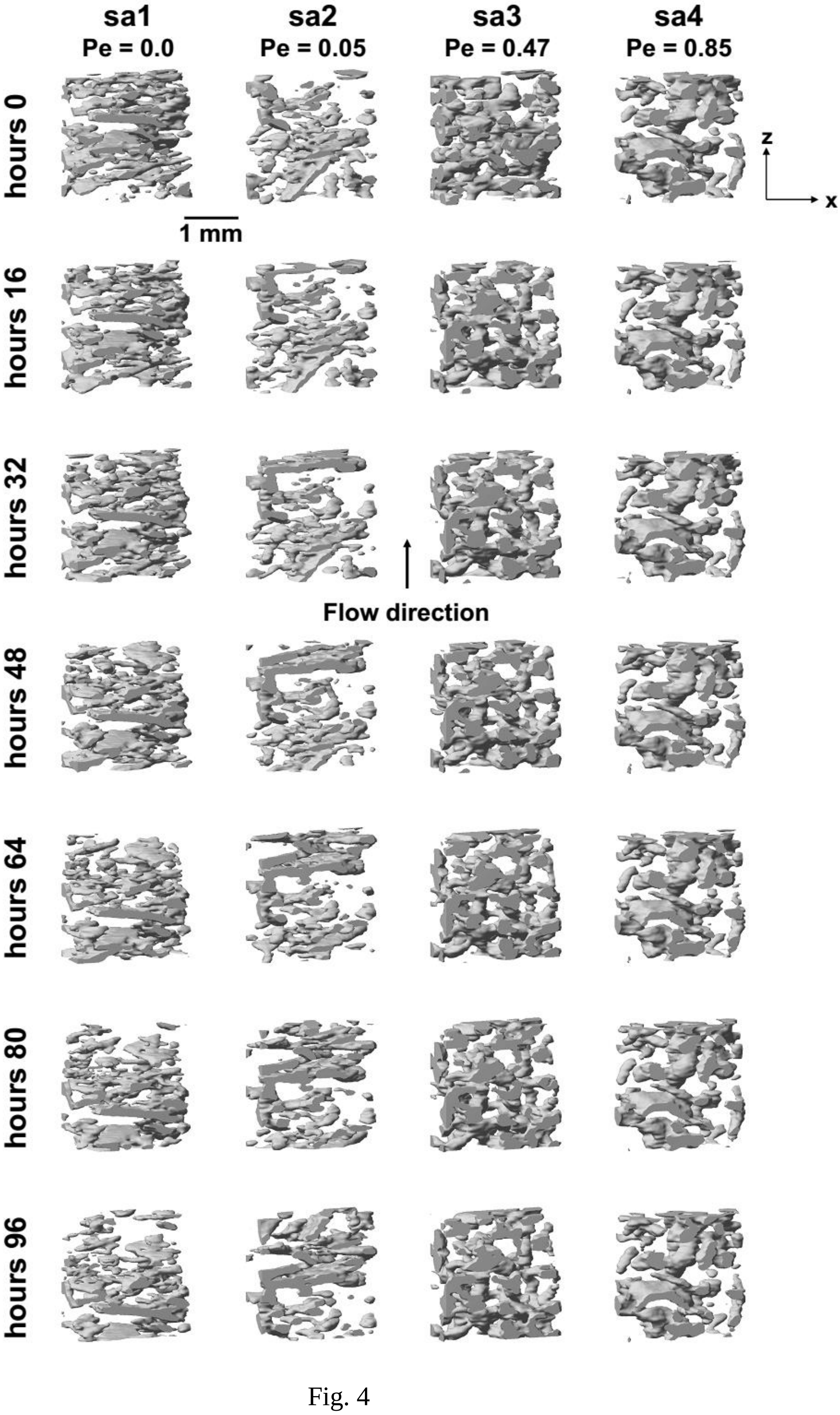
sa1
Pe = 0.0
sa2
Pe = 0.05
sa3
Pe = 0.47
sa4
Pe = 0.85
hours 0
hours 16
hours 32
hours 48
hours 64
hours 80
hours 96
1 mm
z
x
Flow direction

Fig. 4

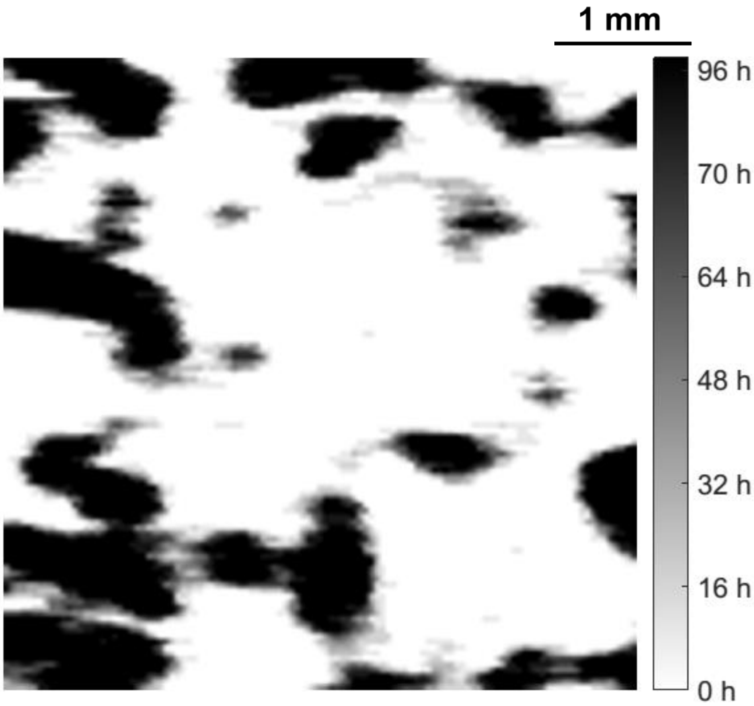

Fig. 5 a)

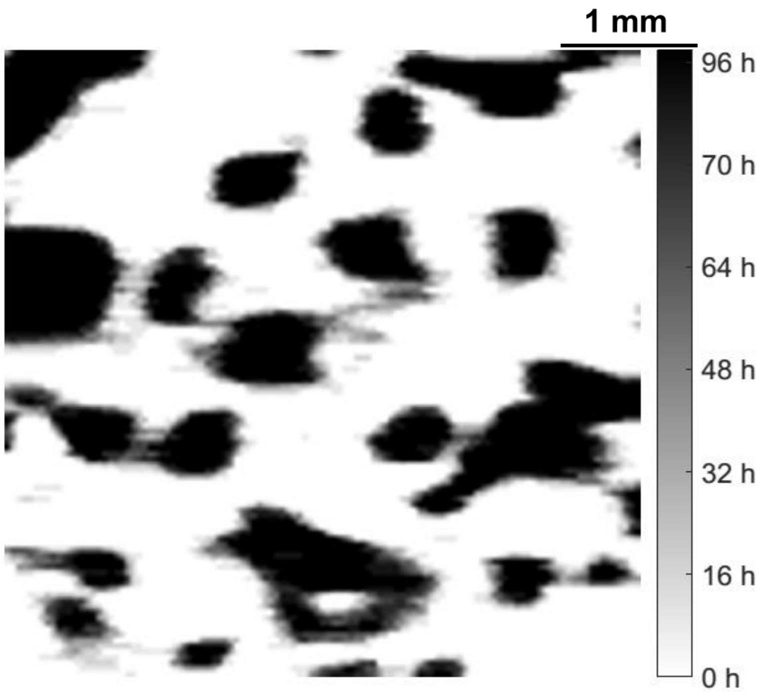

Fig. 5 b)

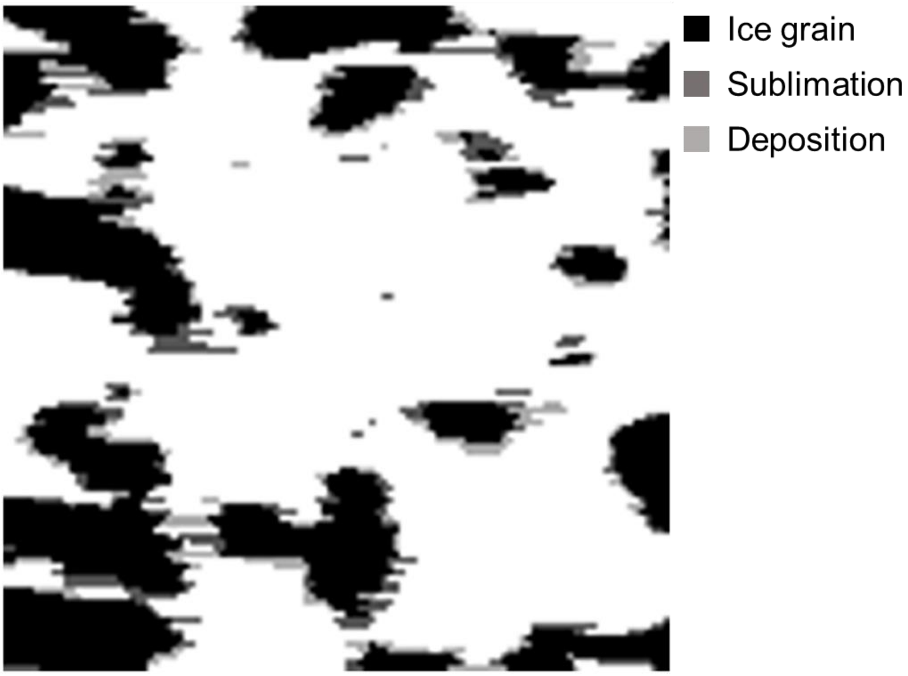

Fig 6 a)

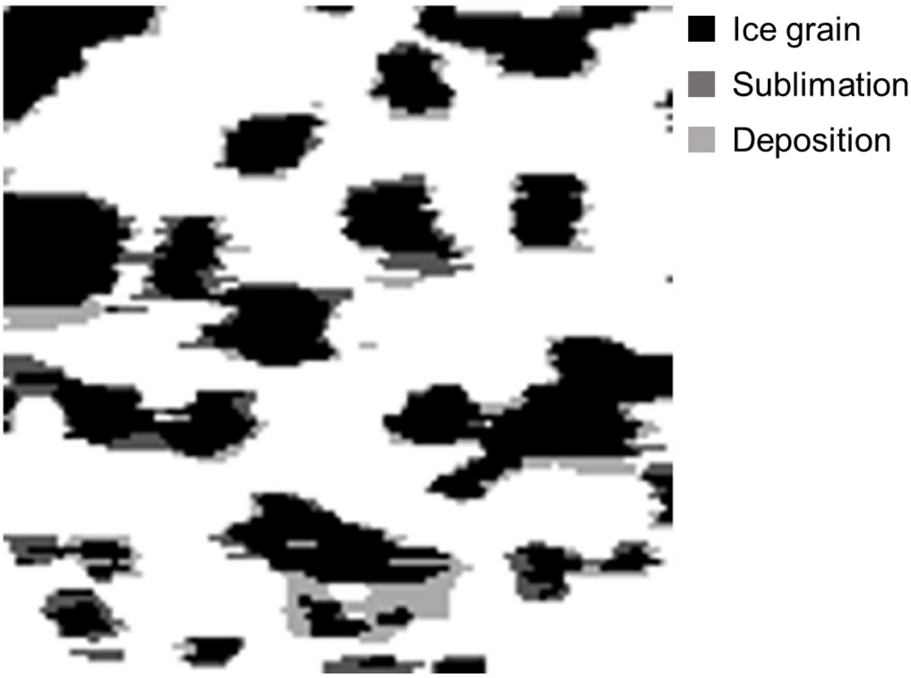

Fig. 6 b)

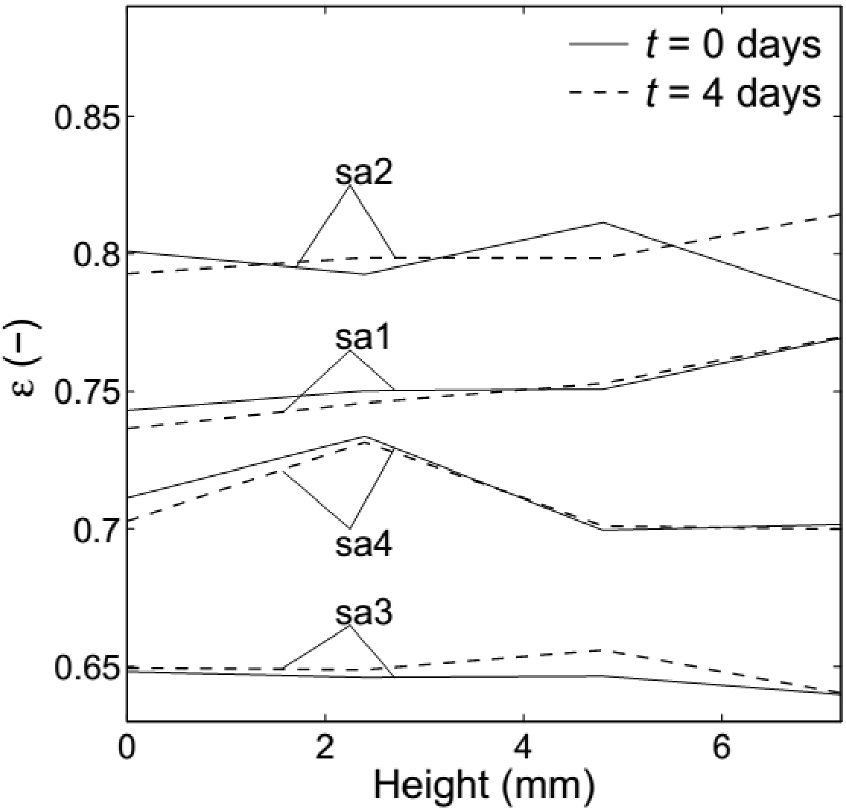
t = 0 days
t = 4 days
0.85
0.8
0.75
0.7
0.65
sa2
sa1
sa4
sa3
ε (–)
0
2
4
6
Height (mm)

Fig. 7

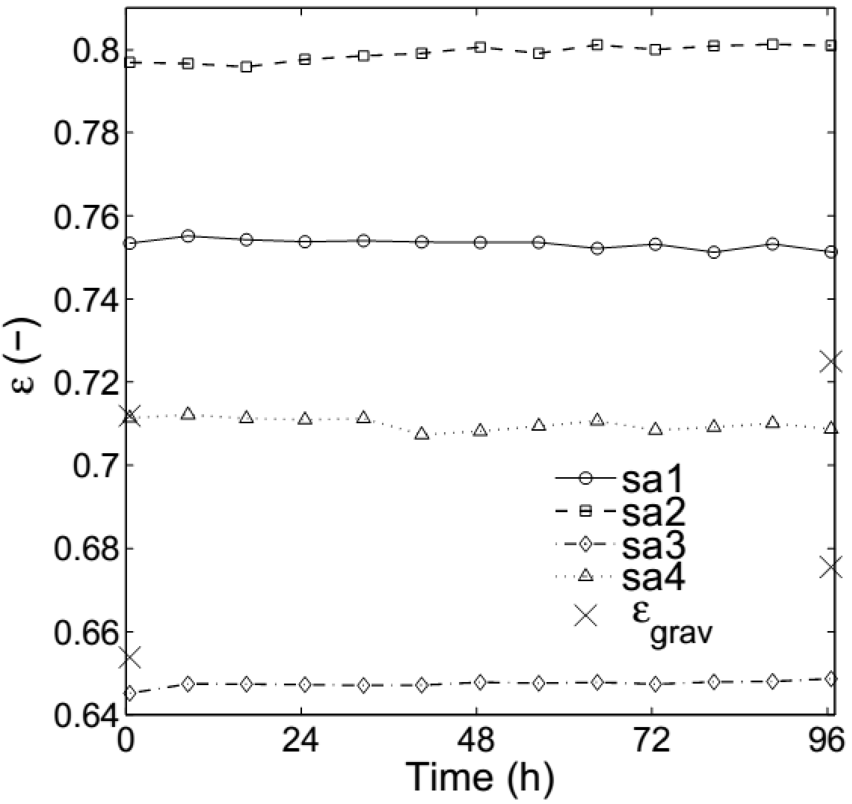
0.8
0.78
0.76
0.74
0.72
0.7
0.68
0.66
0.64
ε (–)
0
24
48
72
96
Time (h)
sa1
sa2
sa3
sa4
ε
grav

Fig. 8

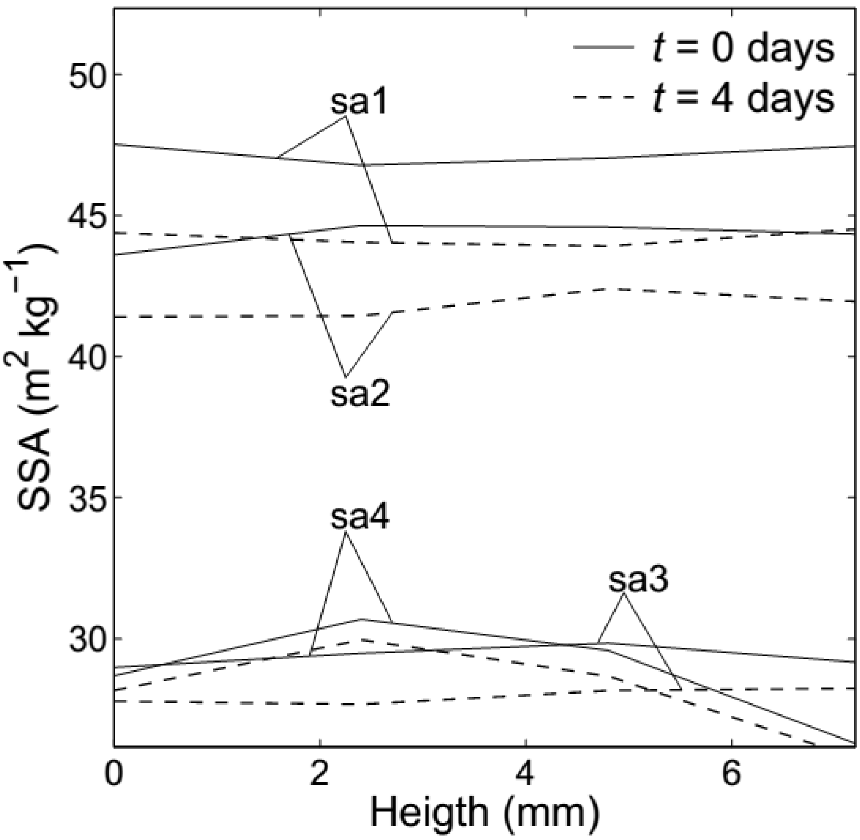
t = 0 days
t = 4 days
sa1
sa2
sa3
sa4
SSA (m2 kg−1)
Heigth (mm)
50
45
40
35
30
0
2
4
6

Fig. 9

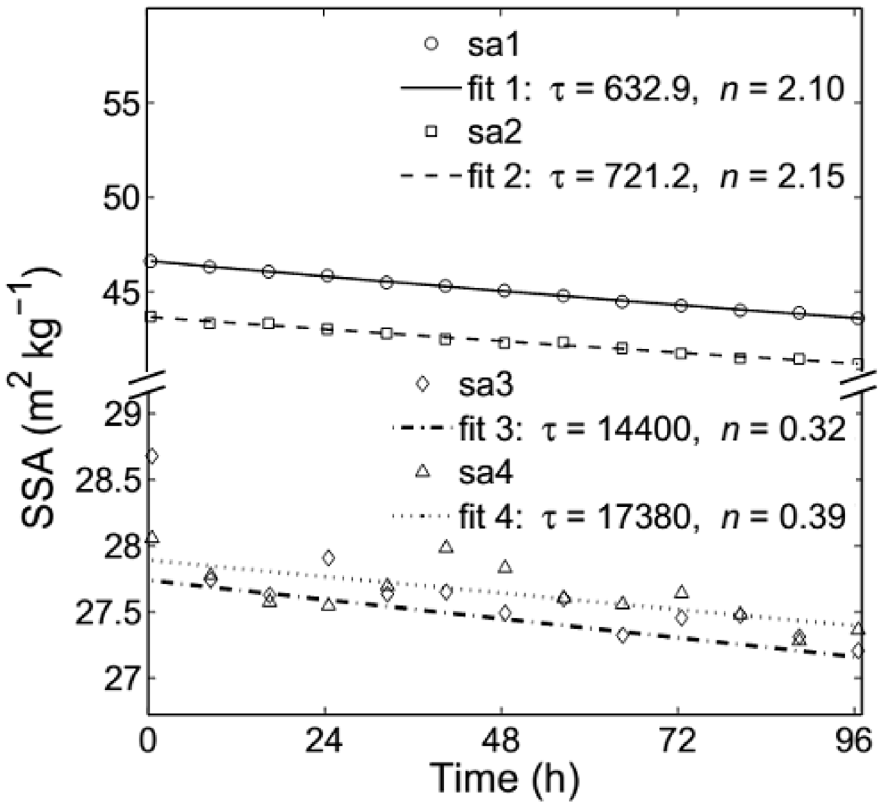
sa1
fit 1: τ = 632.9, n = 2.10
sa2
fit 2: τ = 721.2, n = 2.15
sa3
fit 3: τ = 14400, n = 0.32
sa4
fit 4: τ = 17380, n = 0.39
SSA (m² kg⁻¹)
Time (h)
0
24
48
72
96
55
50
45
29
28.5
28
27.5
27

Fig. 10

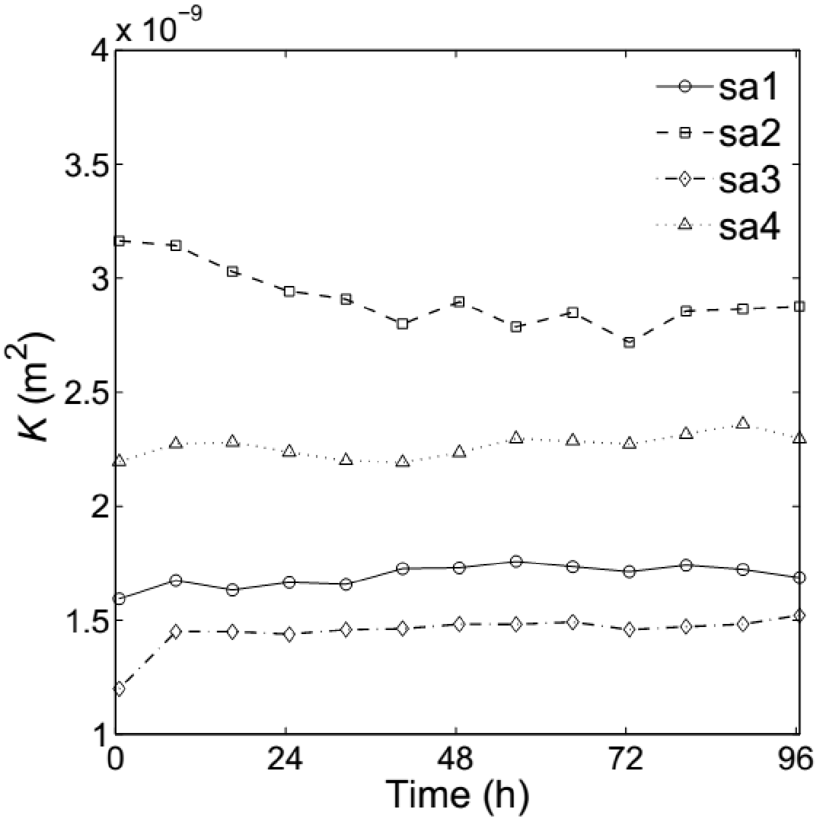

Fig. 11